J. Space Weather Space Clim. 2022, **12**, 18

https://doi.org/10.1051/swsc/2022012

JSWSC

Available online at:
www.swsc-journal.org

RESEARCH ARTICLE OPEN ACCESS

Mesospheric ionization during substorm growth phase

Kiyoka Murase[1,*], Ryuho Kataoka[1,2], Takanori Nishiyama[1,2], Koji Nishimura[10], Taishi Hashimoto[1,2], Yoshimasa Tanaka[1,2,3], Akira Kadokura[1,2,3], Yoshihiro Tomikawa[1,2], Masaki Tsutsumi[1,2], Yasunobu Ogawa[1,2], Herbert Akihito Uchida[5], Kaoru Sato[4], Satoshi Kasahara[4], Takefumi Mitani[5], Shoichiro Yokota[6], Tomoaki Hori[7], Kunihiro Keika[4], Takeshi Takashima[5], Yoshiya Kasahara[8], Shoya Matsuda[8], Masafumi Shoji[7], Ayako Matsuoka[9], Iku Shinohara[5], Yoshizumi Miyoshi[7], Tatsuhiko Sato[12], Yusuke Ebihara[10], and Takashi Tanaka[11]

[1] Department of Polar Science, The Graduate University for Advanced Studies, SOKENDAI, Tachikawa, 190-8518 Tokyo, Japan
[2] National Institute of Polar Research, Tachikawa, 190-8518 Tokyo, Japan
[3] Polar Environment Data Science Center, Research Organization of Information and Systems, Tachikawa, 105-0001 Tokyo, Japan
[4] Department of Earth and Planetary Science, The University of Tokyo, Bunkyo-ku, 113-0032 Tokyo, Japan
[5] Japan Aerospace Exploration Agency, Institute of Space and Astronautical Science, Sagamihara, 252-5210 Kanagawa, Japan
[6] Graduate School of Science, Osaka University, Toyonaka, 560-0043 Osaka, Japan
[7] Institute for Space–Earth Environmental Research, Nagoya University, Nagoya, 464-8601 Aichi, Japan
[8] Graduate School of Natural Science and Technology, Kanazawa University, Kakuma-machi, 920-1192 Ishikawa, Japan
[9] Data Analysis Center for Geomagnetism and Space Magnetism, Kyoto University, Sakyo-ku, 606-8502 Kyoto, Japan
[10] Research Institute for Sustainable Humanosphere, Kyoto University, Uji, 611-0011 Kyoto, Japan
[11] International Center for Space Weather Science and Education, Kyushu University, Fukuoka, 819-0395 Fukuoka, Japan
[12] Japan Atomic Energy Agency, Tokai-mura, 319-1184 Ibaraki, Japan

Received 1 October 2021 / Accepted 20 April 2022

Abstract – Many studies have been conducted about the impact of energetic charged particles on the atmosphere during geomagnetically active times, while quiet time effects are poorly understood. We identified two energetic electron precipitation (EEP) events during the growth phase of moderate substorms and estimated the mesospheric ionization rate for an EEP event for which the most comprehensive dataset from ground-based and space-born instruments was available. The mesospheric ionization signature reached below 70 km altitude and continued for ~15 min until the substorm onset, as observed by the PANSY radar and imaging riometer at Syowa Station in the Antarctic region. We also used energetic electron flux observed by the Arase and POES 15 satellites as the input for the air-shower simulation code PHITS to quantitatively estimate the mesospheric ionization rate. The calculated ionization level due to the precipitating electrons is consistent with the observed value of cosmic noise absorption. The possible spatial extent of EEP is estimated to be ~8 h MLT in longitude and ~1.5° in latitude from a global magnetohydrodynamic simulation REPPU and the precipitating electron observations by the POES satellite, respectively. Such a significant duration and spatial extent of EEP events suggest a non-negligible contribution of the growth phase EEP to the mesospheric ionization. Combining the cutting-edge observations and simulations, we shed new light on the space weather impact of the EEP events during geomagnetically quiet times, which is important to understand the possible link between the space environment and climate.

Keywords: Mesospheric ionization / energetic electron precipitation / substorm / growth phase

1 Introduction

A possible link between the space environment and climate exists when mesospheric ionization occurs due to sub-MeV/MeV electron precipitation, causing ozone depletion in the mesosphere (Miyoshi et al., 2021). These events are known as energetic electron precipitation (EEP) events (Clilverd et al., 2008; Cresswell-Moorcock et al., 2013; Seppälä et al., 2015; Miyoshi et al., 2015; Sivadas et al., 2017; Oyama et al., 2017; Tanaka et al., 2019). The approximate energies for electrons stopping at 65 km and 70 km of the mesospheric altitude are 300 keV

*Corresponding author: murase.kiyoka@nipr.ac.jp

and 200 keV, respectively. This study focuses on such low-altitude mesospheric ionization signatures during EEP events.

Substorm plays a major role in energizing electrons in the magnetosphere and precipitating the energetic electrons into the polar atmosphere (e.g., Jelly & Brice, 1967; Bailey, 1968; Pytte et al., 1976; Miyoshi et al., 2013; Jaynes et al., 2015; Ebihara & Tanaka, 2013). The characteristics and causes of EEP events vary depending on the substorm phase (Kirkwood & Eliasson, 1990; Ranta & Ranta, 1981). For example, during the recovery phase, whistler-mode chorus waves cause EEP events and the dominant ionization at D-region altitude reaching below 70 km altitude (Miyoshi et al., 2015a; Oyama et al., 2017) and resultant ozone depletion at the mesosphere (Miyoshi et al., 2021). Kataoka et al. (2019) reported that the mesosphere at ~65 km was transiently ionized during the expansion onset, although the associated magnetospheric plasma waves were not identified. Sivadas et al. (2019) reported a diffuse auroral arc and mesospheric ionization at an altitude of ~70 km during the substorm growth phase. They interpreted the deep ionization based on the pitch-angle scattering of energetic electrons by the field-line curvature (FLC) in the magnetotail because their observations showed the energy dispersion of the precipitating electrons, as expected from the proposed FLC scattering mechanism (Kirkwood & Eliasson, 1990; Imhof, 1988).

The impacts of EEP events on the atmosphere have been studied during geomagnetically disturbed periods, including the expansion and the recovery phase of the substorm (Goldberg et al., 1984; Baker et al., 1987; Pesnell et al., 1992; Tesema et al., 2020; Bland et al. 2021; Miyoshi et al., 2021). The atmospheric ionization during the growth-phase EEP events has also been reported (Rossberg, 1976; Ranta & Ranta, 1981; Jussila et al., 2004; McKay et al., 2018; Sivadas et al., 2019), whereas the magnitude of the impact of the growth-phase EEP events relative to those in the other phases of the substorm is still an open question.

The present study aims to evaluate the atmospheric impact of sub-MeV electrons during the substorm growth phase by taking a rare opportunity of a conjugate observation campaign between the Arase satellite and the PANSY radar at Syowa Station. Section 2 describes these instrumentations. In Section 3, simulation settings are briefly explained. We show the observation data and quantitative examination via the air-shower simulation in Section 4. The discussions follow in Section 5. Concluding remarks are summarized in Section 6.

2 Observations

2.1 Ground-based observations at Syowa Station

The PANSY radar, the Program of the Antarctic Syowa Mesosphere–Stratosphere–Troposphere/Incoherent Scatter radar, is located at Syowa Station in the Antarctic region (69.0°S, 39.6°E; CGMLAT = −66.5°). The radar has been in full and continuous operation since October 2015. The observation frequency is 47 MHz with five beams in the directions of the local zenith, geographic north, east, south, and west, with the zenith angles of 10°. We mainly examined mesospheric echoes in the winter season (so-called polar mesosphere winter echoes) from March through October. The range resolution in the mesospheric observation is 600 m in winter, and these data

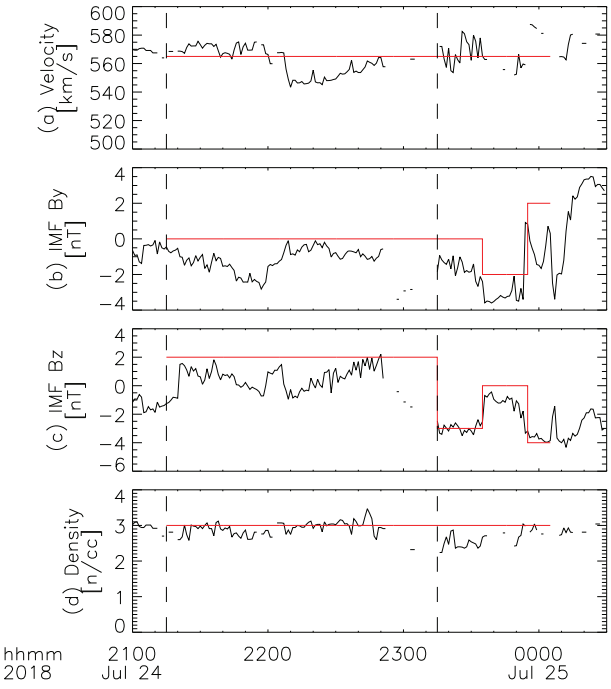

Figure 1. Solar wind parameters during the substorm associated with Event # 1 on July 24–25, 2018. (a) Solar wind velocity, (b) *Y*-, (c) *Z*-components of IMF in GSM coordinate, and (d) density are shown. Red and Black lines represent input parameters to the REPPU simulation, and 1-min OMNI data obtained from https://spdf.gsfc.nasa.gov/pub/data/, respectively.

are obtained every ~4 min (Sato et al., 2014). We used the altitude-resolved mesospheric echo power as a proxy for the increase in the electron density due to EEP (Nishiyama et al., 2015; Kataoka et al., 2019; Tanaka et al., 2019).

Syowa Station is a manned comprehensive geophysical observatory where several different observations are conducted for geophysical studies. The most relevant to this study is the imaging riometer. The imaging riometer measures cosmic noise absorption sensitive to the precipitation of electrons of several tens to several hundreds of keV. The imaging array consists of 8 × 8 beams, covering an area of 180 km × 180 km at 80 km altitude. The observation frequency of the imaging riometer is 38.2 MHz, with an angular resolution of ~10° near the zenith. The data sampling interval is 1 s.

All-sky auroral image data from an Electron-Multiplying Charge Coupled Device camera are also available at Syowa Station (Uchida et al., 2020). The data with the original sampling rate of 100 frames per second were integrated for each second. The resultant 1 s images were used in this study to reduce the random noise and to detect faint emissions associated with EEP. We also consult the fluxgate magnetometer data at Syowa Station to identify the substorm phase. In this study, the growth phase was determined to be a period during which a quiet arc existed without a strong H-component decrease before the expansion onset. The onset was defined by a rapid change of auroras in all-sky images.

Here we explain the event selection of EEP events. First, from a visual inspection of the quick-look plots for the altitude-resolved echo powers observed by the PANSY radar

(http://polaris.nipr.ac.jp/~reppu/nighttime_20-28UT/) for two consecutive winter periods since March 2017, we found 25 events of the nighttime mesospheric ionization below the altitude of 70 km (see Appendix A), which indicated precipitation of electrons of more than 200 keV. The sunlit time was excluded to eliminate ionization events due to sunlight. Out of the 25 events, two had comprehensive datasets from the ground-based observations at Syowa Station during the substorm growth phases.

2.2 Satellite observations

The Arase satellite has conducted in-situ observations of energetic particles and plasma waves in the inner magnetosphere since March 2017 (Miyoshi et al., 2018a). The pitch-angle-resolved energetic electron measurements cover the energy ranges of 7–87 keV with the medium-energy particle experiments–electron analyzer (MEP-e) (Kasahara et al., 2018a, 2018c) and ~70–2000 keV with the high-energy electron experiments (HEP) (Mitani et al., 2018a, 2018b). Plasma waves in the ELF/VLF (0.1–100 kHz) and ULF (0.001–1 Hz) ranges are also simultaneously measured by the onboard frequency analyzer (OFA) of the plasma-wave experiment (PWE) (Kasahara et al., 2018b, 2018d; Matsuda et al., 2018) and magnetic field experiment (MGF) (Matsuoka et al., 2018a, 2018b), respectively.

The Polar Operational Environmental Satellites (POES) 15 is a polar-orbiting satellite at an altitude of approximately 800–900 km. The Medium Energy Proton and Electron Detector (MEPED) onboard POES satellites (Evans & Greer, 2004) measures both horizontal and vertically-downward electron fluxes in three integrated energy ranges of >30 keV, >100 keV, and >300 keV. The flux data are provided with a cadence of 2 sec.

3 Evaluation of the atmospheric ionization

We calculate the atmospheric ionization rate using the particle and heavy ion transport code system (PHITS) (Sato et al., 2018). The Electron-Gamma Shower (EGS5) mode is adopted in the present study (Hirayama et al., 2005). In this study, we use the data of precipitating particle fluxes measured by the Arase and the POES satellite as the inputs for PHITS simulation. We set a simple column-shaped atmosphere. The altitude profile of the atmospheric density and composition at Syowa Station at 0000 UT on July 25, 2018, are provided by the NRLMSISE-00 model (Picone et al., 2002). The altitude resolution is set to 1 km. The incident electrons are assumed to be isotropic at the top of the atmosphere at an altitude of 200 km. The conversion of the observed differential flux into the input flux at the top of the atmosphere is explained in Appendix B.

Global magnetohydrodynamics (MHD) simulation, called a REProduce Plasma Universe (REPPU) code (Tanaka, 2015), was also conducted to estimate the possible spatial extent of EEP events, assuming the pitch angle scattering by FLC. In this study, we derive the equatorial map of the K parameter, the ratio between the curvature radius of magnetic field lines, and the particle gyro radius of given energy (Sergeev et al., 1983). To reproduce the observed moderate substorm of EEP event #1, as shown in Section 4.1, we set the solar wind density at 3.0 cm^{-3}, the speed at 566 km s^{-1}, and the X-component of the interplanetary magnetic field (IMF) at 0.0 nT. The IMF By and Bz are switched to follow the OMNI data, as shown in Figure 1.

We tried several different inputs, such as the OMNI data or a synthetic time series of solar wind parameters approximating the OMNI data. Testing various sets of input parameters, we found that the stable preconditioning of a positive Bz component without the By component, as shown in Figure 1, gives the most similar magnitude and the nearest timing of the onset for the observed substorm. We, therefore, selected the synthetic time series as the best example.

4 Results

4.1 EEP Event #1 on July 24–25, 2018

The first EEP event analyzed in this study has the most comprehensive data sets of ground-based and space-born observations. The EEP event #1 occurred on July 24–25, 2018, during a moderate substorm with the peak SME (SuperMAG electrojet, Gjeloev, 2012) index of ~400 nT. The substorm onset took place at ~0005 UT on July 25, 2018, as determined by the decrease in the H-component of the magnetic field at Syowa Station (Fig. 3e) as well as the rapid change of the aurora (see Movie S1) at −67.5° altitude-adjusted corrected geomagnetic (AACGM) latitude (Shepherd, 2014). Throughout this event, the footprint of the Arase satellite, as calculated with the T96 (Tsyganenko, 1996) model (Fig. 2), was located approximately 1 h later in MLT than at Syowa Station. During the late growth phase, the Arase footprint approached closest in latitude to the Syowa Station at ~0000 UT, and the footprint of the POES-15 satellite also passed the same magnetic latitude as Syowa Station at ~2357 UT (Fig. 2). We confirmed that the difference in the mapped positions between the different versions of the Tsyganenko model is negligible for the following discussions, as expected from non-storm time conditions.

Figure 3 shows an overview of the ground-based observations at Syowa Station. The PANSY radar detected a transient mesospheric echo extending from ~80 km down to ~68 km during the growth and early expansion phase from 23:57:31 UT to 00:06:10 UT (Fig. 3a). This echo enhancement was associated with the increase in CNA around the zenith at the same time (Figs. 3b and 3c). Note that the maximum echo power is shown here because it is a better parameter than the average power correlated with CNA. The east-west aligned arc of CNA was located slightly poleward of the beam directions of the PANSY radar (Figs. 3f and 3g) and continued to appear in the FOV of the imaging riometer for 15–20 min until the onset of the substorm at ~0005 UT. The maximum CNA value was ~0.5 dB during the growth phase.

Figure 4 shows the dynamic spectra of the magnetic field and energetic electron fluxes as observed by the Arase satellite. The loss-cone flux measured by MEP-e was enhanced at ~0003 UT during the late growth phase (Fig. 4f). The loss-cone flux was almost comparable to the trapped one in the energy range of <20 keV at that time. The Arase satellite detected significant variations in the wave activity after the

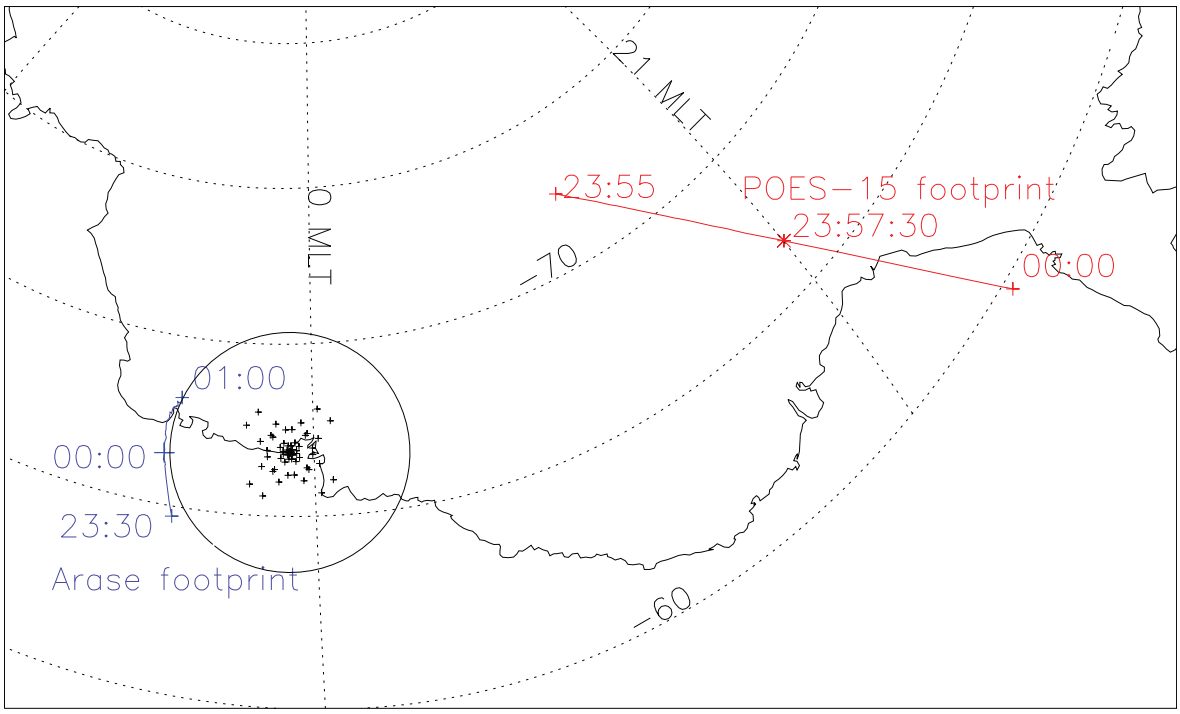

Figure 2. Footprints of (blue) the Arase and (red) the POES-15 satellites during the EEP event #1 on July 24–25, 2018, in the AACGM coordinate. The mapped altitude is 100 km for both satellites. The magnetic local times are calculated at 0000 UT. The footprints of the Arase and the POES satellites were traced using the T96 model. The black circle indicates the all-sky field of view at Syowa Station, assuming a 10° elevation angle and an emission altitude of 110 km. Plus signs show the 8×8 beam directions of the imaging riometer, projected at 90 km altitude.

substorm onset, although there are no wave activities during the growth phase (Figs. 4a–4b).

At the same timing when the PANSY radar detected the ionization at <70 km (Fig. 3a), the POES-15 satellite has passed through the same magnetic latitude at ~3 MLT away from Syowa Station (Figure 2), moving equatorward at an altitude of 840 km. The latitudinal extent of the electron precipitation was estimated to be ~1.5° (Figs. 5b–5d), which is consistent with the typical characteristics of EEP by FLC scattering during the growth phase (Sivadas et al., 2019; Sergeev et al., 2012; Pytte et al., 1976).

In order to evaluate the altitude profile of the mesospheric ionization rate, we show the inputs and outputs of the PHITS simulation in Figure 6. Figure 6a shows the differential fluxes of electrons measured by the Arase satellite and POES 15 during the growth phase. The electron fluxes measured by MEP-e (loss-cone flux) and HEP-L (flux at pitch angle >160°) of the Arase satellite were averaged over a 5-min period from 0000 UT on July 25, when MEP-e observed the increase of loss-cone fluxes. Note that the flux for HEP-L gives the upper limit of precipitating fluxes because it is not possible to measure only the flux inside the loss cone with the angular resolution of the HEP-L. The flux outside the loss cone is included, so the flux at pitch angle >160° is expected to be larger than the flux inside the loss cone. Even using the loss-cone flux of MEP-e also gives the upper limit because of the low count rate (low S/N ratio) in which the contribution of background noises cannot be neglected. We also show the flux measured by MEPED of the POES 15 at 2357:30 UT on July 24, when the vertical electron flux peaked. The differential fluxes at 30–100 keV and 100–300 keV were calculated from the difference between the >100 keV flux and the >30 keV flux and the difference between the >300 keV flux and the >100 keV flux, respectively. Using these inputs, the ionization rates associated with these precipitating electrons were calculated from the energy deposition into the atmosphere using the PHITS simulation (Fig. 6b). The statistical error of the estimated ionization rate was <1% above 75 km altitude, while <40% below 60 km altitude.

We further evaluate the CNA amplitude from the simulated ionization rate shown in Figure 6b, using the same formulation as that employed by Kataoka et al. (2019), that is, CNA [dB/m] = $4.6 \times 10^{-5}\, \nu\omega^{-2}\, q^{0.5} a^{-0.5}$, where ν, ω, q, and a represent the collision frequency, the observation frequency, the ionization rate, and the recombination coefficient, respectively. The recombination coefficient was obtained from Gledhill (1986), and the collision frequency was obtained from Aggarwal et al. (1979). The CNA amplitudes are estimated to be 0.34 dB and 0.51 dB by considering the fluxes of MEP-e and HEP-L of the Arase satellite, respectively. There is, therefore, a discrepancy between the estimated CNA and the observed one. We interpret that this dB estimate of CNA for the HEP-L range is far too large, and the actual HEP-L contribution must be an order of magnitude smaller, as expected from the discontinuity in the MEP-e and HEP-L fluxes in Figure 6a. The calculated CNA due to the contribution of the MEP-e loss-cone flux alone is sufficient to explain the observed ~0.4 dB (Fig. 3b). The calculated CNA due to MEPED/POES-15 is

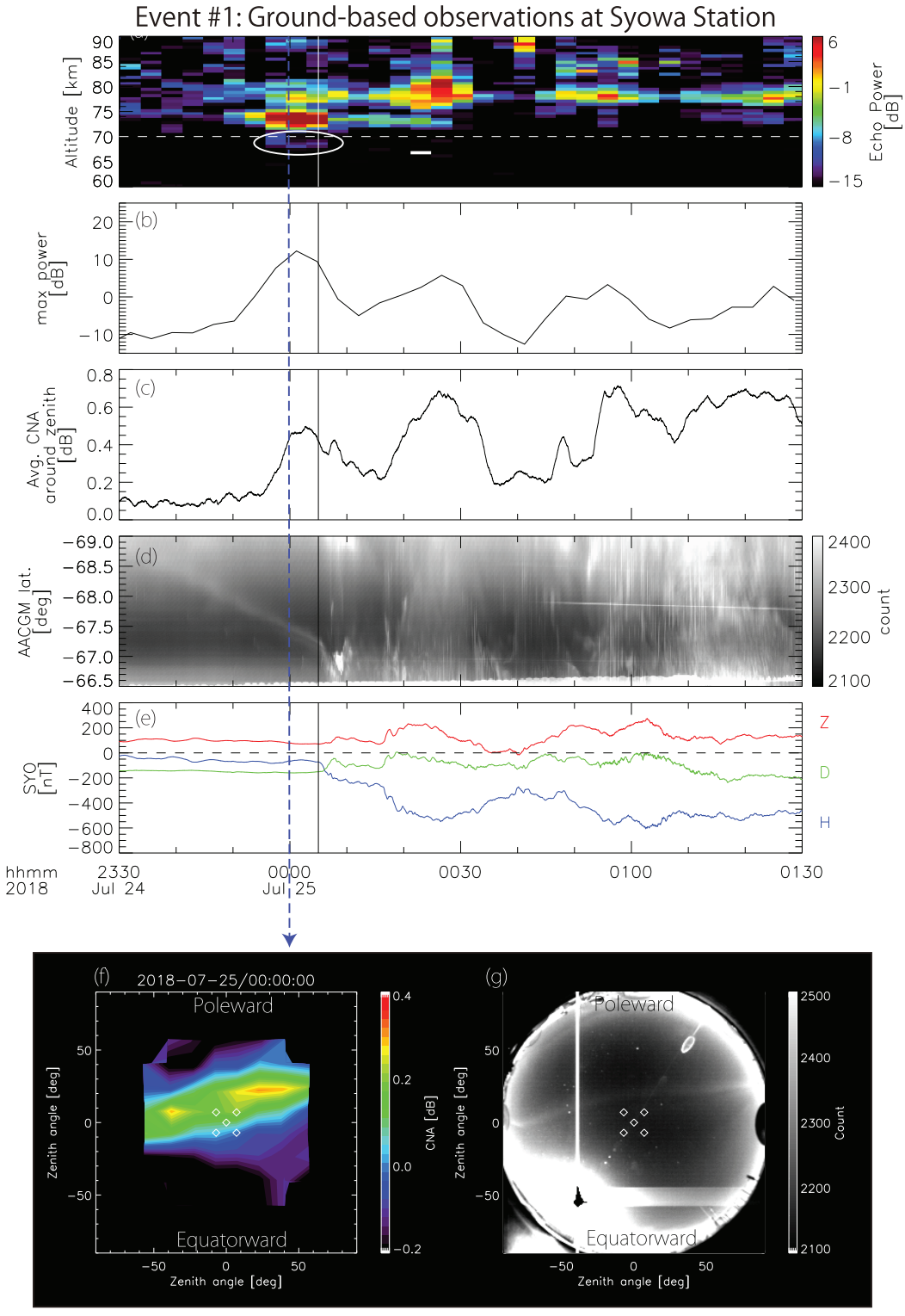

Figure 3. Ground-based observations at Syowa Station of the EEP event #1 for a 2-hour period from 2330 UT on July 24, 2018. Shown are the (a) time-varying altitude profile of the echo power as observed by PANSY, (b) time variation of the maximum echo power as calculated from panel (a), (c) CNA at the zenith as observed by the imaging riometer, (d) north-south variation of the aurora, and (e) magnetometer data. The white ellipse in (a) marks the echo at <70 km. The white areas in (a) represent the data gaps. The CNA in panel (c) was averaged over the four beams of the imaging riometer around the zenith and then smoothed with a two-minute moving average. The solid vertical line indicates the beginning of the expansion phase of the substorm. The bottom panels show the all-sky maps of (f) CNA and (g) aurora at 0000 UT on July 25, 2018, indicated by the blue dotted line. The white diamonds in the bottom panels represent the beam directions of the PANSY radar. Note that the bright signatures in the lower left and upper right portions are the contamination from moonlight and its reflection.

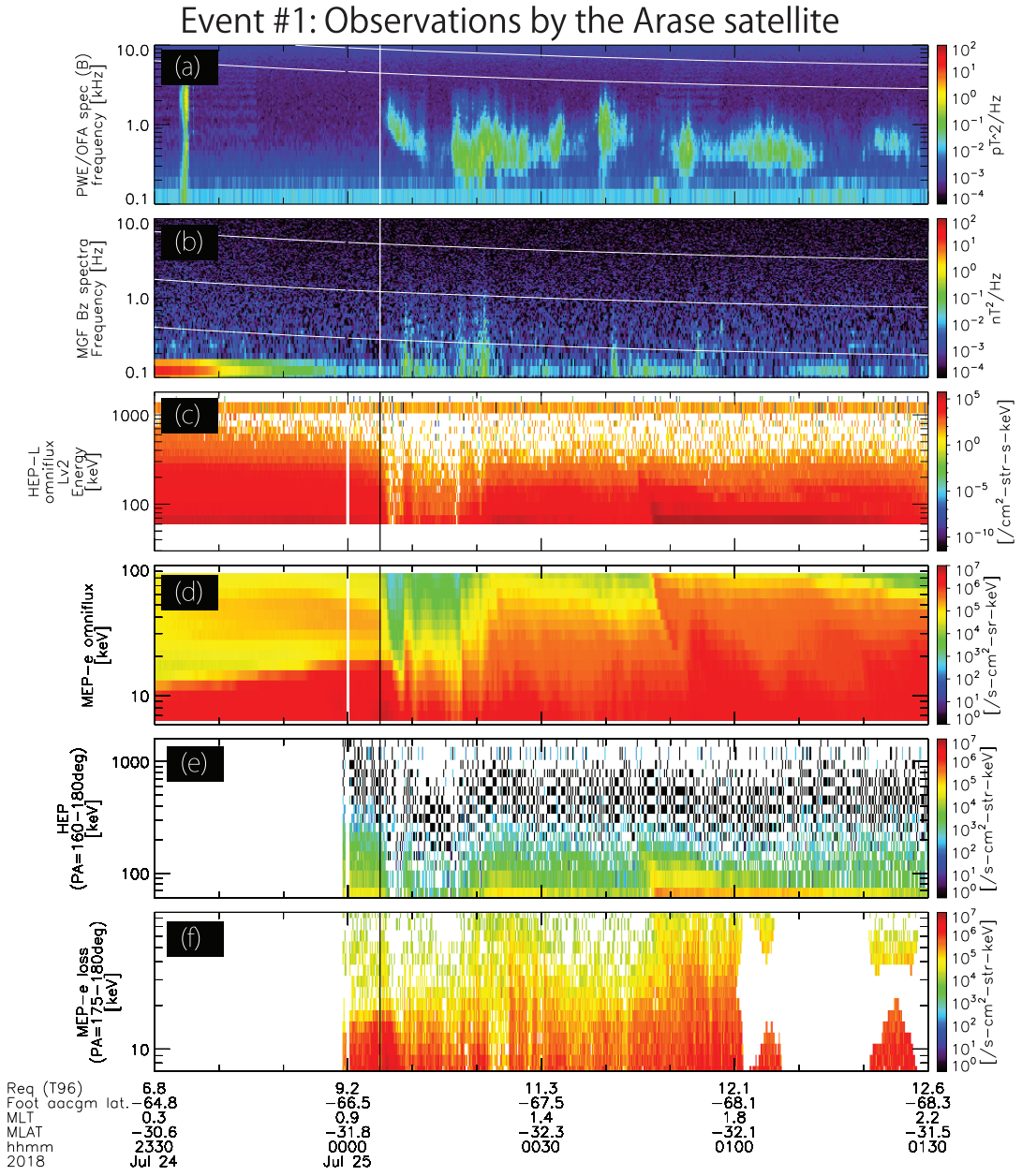

Figure 4. In-situ observation of plasma waves and energetic electrons at the Arase satellite for the same time period as shown in Figure 3. The vertical solid line at 0005 UT indicates the onset of the substorm. The top two panels show frequency-time spectra of the wave magnetic field measured by (a) PWE-OFA and (b) MGF. The solid white curves in (a) represent f_{ce} and 0.5 f_{ce}, respectively, where f_{ce} is the local electron cyclotron frequency. The white curves in (b) represent the O^+, He^+, and H^+ cyclotron frequencies, respectively, as calculated from the local magnetic field measured by MGF. Energy-time spectra of the omnidirectional electron fluxes observed by (c) HEP-L and (d) MEP-e are shown in the middle. The pitch-angle resolved fluxes as measured by (e) HEP-L and (f) MEP-e are also shown. The loss-cone angle was calculated to be 4.9° at the Arase satellite position at 0005 UT. The labels "Req (T96)" and "Foot aacgm lat" represent the geocentric distance of the magnetic equator and AACGM latitude of the footprints in the southern hemisphere, respectively, both traced from the position of the Arase satellite using the T96 model.

0.39 dB, which is consistent with the observed one, although the satellite was 3 MLT away from Syowa Station.

4.2 EEP Event #2 on May 25–26, 2017

Figure 7 shows an overview of the ground-based observations at Syowa Station on May 25–26, 2017. This event occurred during a moderate substorm in which the peak value of the SME index was ~200 nT. The substorm onset took place at ~2325 UT when the auroral activity appeared in the poleward portion of the all-sky field of view (>|−68°| AACGM latitude) (Fig. 7d and Movie S2) and the *Z*-component of the local magnetic field increased (Fig. 3e), indicating the increase of the auroral electrojet on the poleward side of Syowa Station.

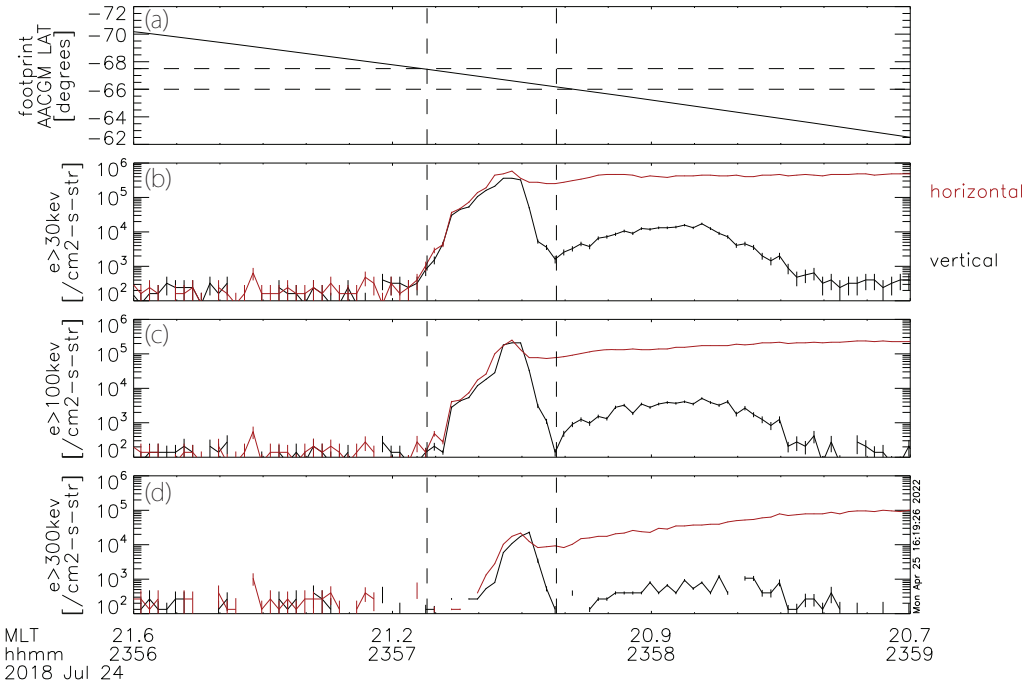

Figure 5. POES-15 observational data for 3 min from 2356 UT on July 24, 2018. (a) Magnetic latitude of the footprint. Integrated number fluxes of electrons in the energy range of (b) >30 keV, (c) >100 keV, and (d) >300 keV. Black and red lines represent vertical and horizontal electron fluxes, respectively. Vertical dashed lines mark 2357:07 UT and 2357:37UT.

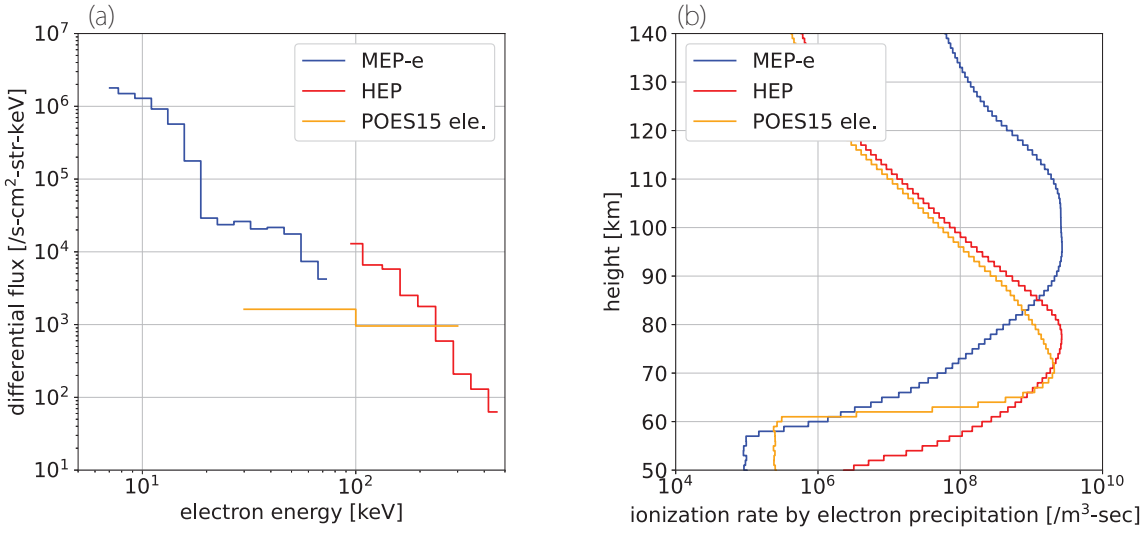

Figure 6. (a) Differential flux of electrons as measured by (blue) MEP-e and (red) HEP-L onboard the Arase satellite, and (orange) MEPED onboard the POES-15 during the growth phase. (b) Altitude profiles of the ionization rate as obtained from the PHITS simulation.

Transient mesospheric echoes below 70 km were detected by the PANSY radar in the growth (at 68.1 km altitude) and expansion phases (at 69.3 km altitude), as shown by white ellipses in Figure 7a. The time range was 23:06:35–23:11:15 UT and 23:29:38–23:34:19 UT. At 2307 UT, during the growth phase, when the first transient echo was detected at <70 km altitude, the CNA arc was located poleward of the beam directions of the PANSY radar (Fig. 7f). The arc persisted for ~15 min from ~23:02 UT. Note that during the growth phase, the footprint of the Arase satellite was located at the same MLT region as and ~5° equatorward in the AACGM latitude from Syowa Station. The Arase satellite did not observe chorus or electro-magnetic ion cyclotron waves, which can cause EEP (see Appendix C). The mesospheric echoes at altitudes above 70 km continued to appear for ~4 h from ~2300 UT, and the maximum echo power (Fig. 7b) exhibited a similar time variation with the CNA of the near-beam directions (Fig. 7c).

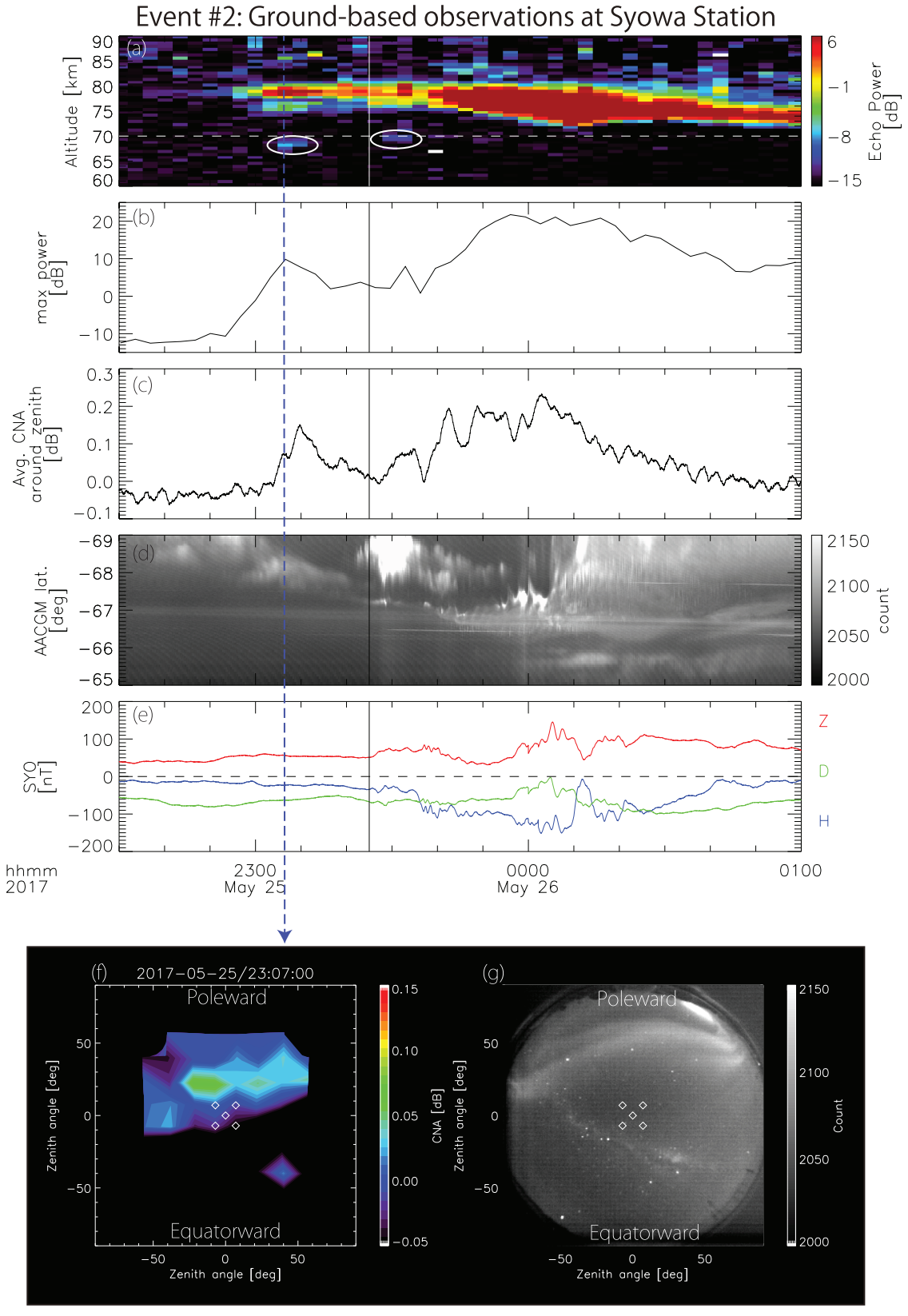

Figure 7. Ground-based observations at Syowa Station of Event #2 for a 2.5-hour period from 2230 UT on May 25, 2017. Top panels (a)–(e) are shown in the same format as Figure 3. The vertical line at 2325 UT indicates the beginning of the expansion phase of the substorm. The bottom panels show the all-sky maps of (f) CNA and (g) aurora from the ground view at 2307 UT, as indicated by the blue dotted line. The white diamonds represent the beam directions of the PANSY radar.

5 Discussions

We reported two substorm-related EEP events during the campaign observations between Syowa Station and the Arase satellite, especially when the mesospheric ionization was identified by the PANSY radar at <70 km altitude. It is notable that the substorm intensity is not strong, and the EEP events occurred during the growth phase before the subsequent auroral breakups or substorm onset. This finding indicates that we have to carefully take into account the atmospheric ionization impacts even during the geomagnetically quiet times. The identified mesospheric echo at <70 km was not persistent, probably due to the limited beam directions of the PANSY radar, which have overlapped only for a few minutes with the narrow latitudinal ionization during the growth phase. We also showed that the contribution of <100 keV electron can explain the observed CNA of ~0.4 dB by the ionization at the altitude of >75 km in Event #1.

Note, however, that any transient appearance of the PANSY echoes does not necessarily imply transient ionization. This study relies on the echo power of the PANSY radar to identify an ionization signature in the mesosphere. The time variation of the echo power tends to show a similar variation with CNA, which is consistent with previous studies suggesting that the enhancement of echo power is frequently detected when energetic particles precipitate into the D region during solar proton events (Kirkwood et al., 2002; Nishiyama et al., 2015). Still, the caveat should be reminded that the echo power is also influenced by the existence of neutral atmospheric turbulence (Yamamoto et al., 1987; Lübken et al., 2007; Nishiyama et al., 2018), which can make the appearance and disappearance of echoes, irrespective to the ionization.

We discuss that the observed signatures of growth-phase EEP events at <70 km altitude are consistent with the FLC mechanism, based on the following reasons. First, the Arase satellite did not detect significant activities of plasma waves in the magnetosphere in both events. Second, in both events, the criteria for FLC scattering are satisfied for sub-MeV electrons precipitating within the field-of-view of the Syowa Station by using T96 tracing. The field lines were traced from the Syowa Station to the magnetic equator using the T96 model, and the curvature radius of the field lines at the equator was estimated. The criteria used here is that the K parameter, the ratio between the curvature radius of magnetic field lines and the particle gyro radius of a given energy, is less than 8 (e.g., Sergeev et al., 1983). Third, lower energy particles precipitated at higher latitudes, which was an expected energy dispersion from FLC scattering. The energy dispersion can be seen by comparing the PANSY and the riometer data: When the PANSY radar detected ionization below 70 km due to EEPs at >200 keV, the CNA arcs indicating EEPs at >10 keV were located on the poleward side of the radar beam directions in both events (Figs. 3f and 7f).

To discuss the spatial extent of growth-phase EEP events, we use a global MHD simulation called REPPU code (Tanaka, 2015) and attempt to reproduce the substorm of Event #1. The simulated maximum AE was ~400 nT, which was comparable to the maximum SME index of the event. The timing of the onset occurred ~10 min earlier in the simulation compared to the observed substorm. The spatial extent of EEP can be estimated with the global MHD simulation by constructing an equatorial map of the K parameter. Figure 8 shows a simulated equatorial map of the K parameter for equatorially mirroring electrons with an energy of 100 keV. The bluish regions satisfy the criteria for FLC scattering, i.e., K parameter less than 8. The region of low K values azimuthally extends over ~8 h in MLT. The ionospheric footprints of the eastern edge (10 R_E, 4 MLT), midnight (8 R_E, 0 MLT) and the western edge (10 R_E, 20 MLT) of the region are (69.3°, 4.3 MLT), (67.4°, 0.0 MLT) and (69.2°, 20.0 MLT), respectively. The simulation result is consistent with the simultaneous observations made by the POES satellite at ~21 MLT and at Syowa Station at ~0 MLT which ensured the minimum extent of ~3 h in MLT. As far as we have examined, the longitudinal extent does not significantly depend on input parameters. Note that the longitudinal extent of ~8 h in MLT is not definitive since physical processes determining the longitudinal extent are unknown. Systematic studies must be done in the future to evaluate the actual variance of the azimuthal extent, including the effects of each component of the IMF.

Here we roughly estimate the total atmospheric impact of the growth-phase EEP events. Assuming that the longitudinal and latitudinal extent of pulsating auroras is 4–5 h in MLT and ~4°, respectively (Bland et al., 2021), the longitudinal extent of growth-phase EEP events (~8 MLT, see Fig. 8) can be ~2 times larger than that of pulsating auroras, while the latitudinal extent (~1.5°, see Fig. 5) is ~2 times smaller than that of pulsating auroras. The duration of the growth-phase EEP events can be estimated to be only ~30 min, which is ~4 times shorter than the typical one of pulsating auroras (Nishimura et al., 2020). In total, the spatial extent multiplied by the duration of growth-phase EEP events can be roughly a quarter of the EEP events associated with pulsating auroras. Assuming that the sub-MeV electron fluxes in the growth phase and the recovery phase are approximately the same, and further considering the relatively high occurrence of moderate substorm events compared to the strong events with strong pulsating auroral activity, the growth-phase EEP events can make a significant contribution to the total mesospheric ionization. This rough estimate, however, should be examined by a careful statistical analysis in the future.

In this study, we partly consult the result of the REPPU simulation about the longitudinal extent of the FLC. However, about the latitudinal width of 100 keV electrons, the mapped footprint area of K<8 is ~0.5° at 21 MLT, narrower than the observed value (~1.5°) by the POES satellite. Further careful study is therefore needed to examine this inconsistency before utilizing the MHD simulation to accurately estimate the FLC-related precipitation.

The number of identified events for each phase (Table A1 in Appendix A) may be biased. From this study, it is clear that the PANSY radar must be situated at the very right place to observe the latitudinally narrow structure of growth-phase EEP events, in contrast to the wide structure of the expansion phase and recovery phase events. The relatively small number of events during the growth phase can be interpreted as a biased selection result, and it does not necessarily mean that growth phase phenomena are less frequent.

The non-negligible contributions of the growth-phase EEP events to the mesospheric ionization are missed in EEP models depending on the geomagnetic activity indices such as the

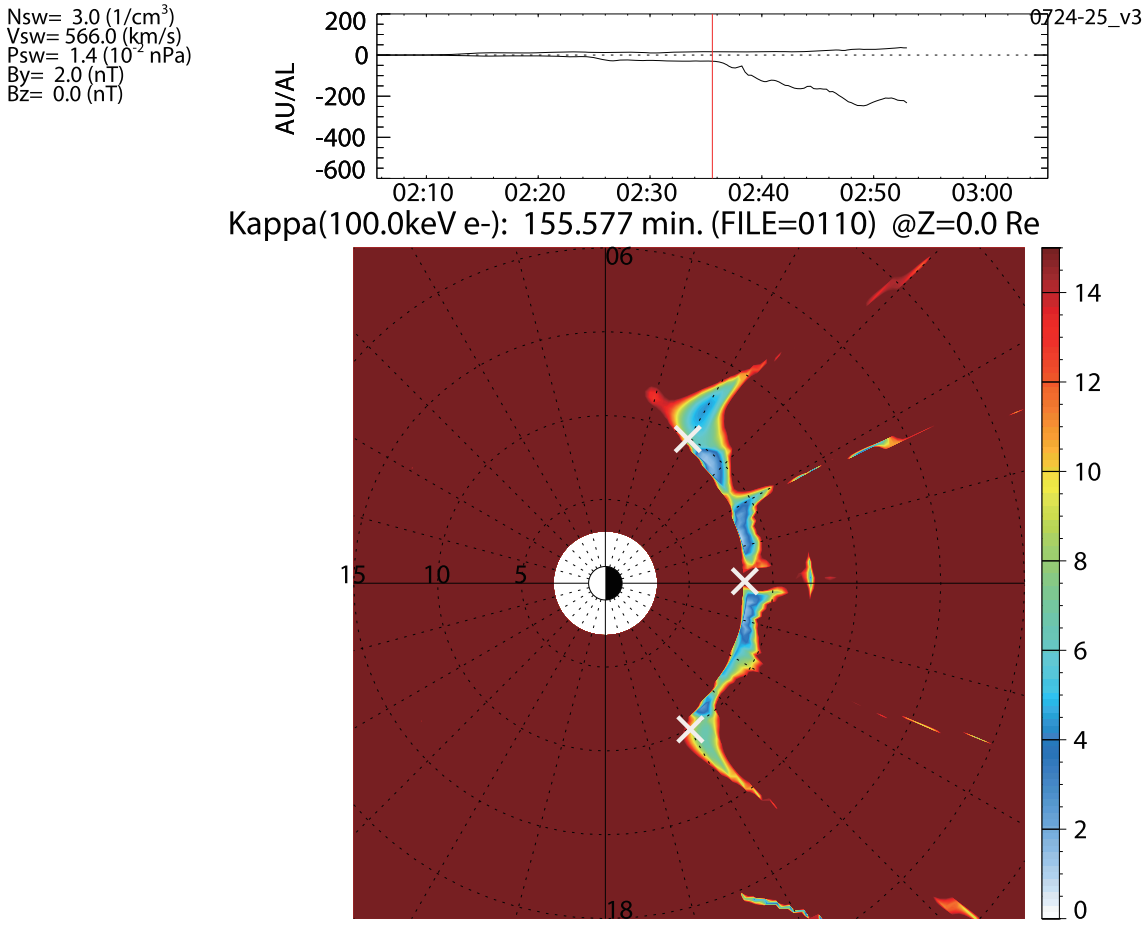

Figure 8. An equatorial map of K parameter for 100 keV electron ~2 min before the auroral breakup. Crosses mark the inner boundaries of the regions at the eastern edge, midnight, and the western edge. The settings of the input solar wind parameters are shown in Figure 1. The top panel shows the simulated AE/AL indices. The time stamps here are irrelevant to the actual event. The sun is to the left.

Ap index because the EEP events usually occur before a geomagnetically active period starts. It is also notable that the contributions of growth-phase EEP events are underestimated even in the empirical model using the POES satellites (e.g., van de Kamp et al., 2018) because the ~90 min orbital period is too long to guarantee that the satellite crosses the growth-phase EEP events.

This study focused on relatively low-altitude echoes to understand the possible impact of the most energetic electrons during substorms. Ongoing research must include the less energetic electrons impacting the higher altitude of the mesosphere. For future work, a superposed epoch analysis of the mesospheric echo profiles referring to substorm onset as the zero epoch would be helpful to quantify the higher-altitude ionization by less-energetic electrons during the different phases of a substorm, depending on the amplitude of substorms, seasons, sunlit conditions, etc.

From the perspective of the space weather forecast, there is another interesting point we can learn from the future detailed comparison between MHD simulation results and the growth phase EEP events occurring near the onset. Some of the global MHD simulations, including the present one, indicate that the rapid thinning of the near-tail plasma sheet precedes the onset signatures in the ionosphere by a few minutes (Ebihara & Tanaka, 2013). Hence the detection of EEP possibly allows us to diagnose the pre-onset state of the near-Earth plasma sheet, utilizing sub-MeV precipitating electrons scattered by the FLC. Further, in addition to such near-onset EEP events, the full evolution of growth-phase EEP events may also shed new light on predicting the substorm amplitude in advance.

6 Conclusions

The mesospheric ionization signatures during the growth-phase EEP events reached <70 km altitude, and the ionization events can continue for at least 15 min. Considering the duration and the spatial extent of the growth-phase EEP events, we suggest that its contribution to the total ionization amount can be significant compared to that during the other substorm phases. This paper first provides the quantitative estimate of the relative impact of the growth-phase EEP events to those in different substorm phases. In order to understand the total atmospheric impact of EEP events, it is, therefore, necessary to clarify the global development of growth-phase EEP events in more detail and quantify those variations in a statistical manner.

Supplementary material

Supplementary material is available at https://www.swsc-journal.org/10.1051/swsc/2022012/olm

Movie S1: Panchromatic all-sky images of Event #1 on July 24–25, 2018, were obtained from the Electron-Multiplying Charge Coupled Device (EMCCD) camera at Syowa Station. Magnetic south is at the top, and magnetic east is to the right. The original sampling rate was 100 frames per second, and all the images were averaged every 1 s to reduce the effective time resolution and random noise. The movie plays at 60 averaged images per second. The PANSY radar's beam positions of local zenith, geographic north, east, south, and west are shown by crosses.

Movie S2: Panchromatic all-sky images of Event #2 on May 25–26, 2017. Formats are the same as Movie S1.

Acknowledgements. PANSY is a multi-institutional project with a core of the University of Tokyo and the National Institute of Polar Research. The PANSY radar observation data are available at the project website, https://pansy.eps.s.u-tokyo.ac.jp (https://doi.org/10.17592/002.2020070384). The Arase satellite data were downloaded and analyzed using the SPEDAS software (http://spedas.org) with the IUGONET and ERG plugins. The redistribution of ground-based observational data has been supported by the IUGONET (Inter-university Upper atmosphere Global Observation NETwork) project. Science data from ERG (Arase) satellite were obtained from the ERG Science Center operated by ISAS/JAXA and ISEE/Nagoya University (https://ergsc.isee.nagoya-u.ac.jp/, Miyoshi et al. 2018b). The present study used the PWE/OFA L2 v02_01 (Kasahara et al., 2018c), MGF L2 v03.03 (Matsuoka et al., 2018b), HEP L2 v03_01 (Mitani et al., 2018b), MEP-e L2 v01_01 (Kasahara et al., 2018d), and ERG Orbit L2 v03 (Miyoshi et al., 2018c). We gratefully acknowledge the SuperMAG collaborators (https://supermag.jhuapl.edu/info/?page=acknowledgement). This work is supported by JSPS-KAKENHI (15H05747, 16H06286, 17H00728, 20H01955, 20H01959, 20K14546). The editor thanks two anonymous reviewers for their assistance in evaluating this paper.

References

Aggarwal KM, Nath N, Setty CSGK. 1979. Collision frequency and transport properties of electrons in the ionosphere. *Planet Space Sci* **27**: 753–768.

Bailey DK. 1968. Some quantitative aspects of electron precipitation in and near the auroral zone. *Rev Geophys* **6(3)**: 289–346. https://doi.org/10.1029/RG006i003p00289.

Baker DN, Blake JB, Gorney DJ, Higbie PR, Klebesadel RW, King JH. 1987. Highly relativistic magnetospheric electrons: A role in coupling to the middle atmosphere? *Geophys Res Lett* **14(10)**: 1027–1030. https://doi.org/10.1029/GL014i010p01027.

Bland E, Tesema F, Partamies N. 2021. D-region impact area of energetic particle precipitation during pulsating aurora. *Ann Geophys* **39**: 135–149. https://doi.org/10.5194/angeo-39-135-2021.

Clilverd MA, Rodger CJ, Brundell J, Bähr J, Cobbett N, Moffat-Griffin T, Kavanagh AJ, Seppälä A, Thomson NR, Friedel RHW, Menk FW. 2008. Energetic electron precipitation during substorm injection events: High-latitude fluxes and an unexpected midlatitude signature. *J Geophys Res* **113**: A10311. https://doi.org/10.1029/2008JA013220.

Cresswell-Moorcock K, Rodger CJ, Kero A, Collier AB, Clilverd MA, Häggström I, Pitkänen T. 2013. A reexamination of latitudinal limits of substorm-produced energetic electron precipitation. *J Geophys Res (Space Phys)* **118**: 6694–6705. https://doi.org/10.1002/jgra.50598.

Ebihara Y, Tanaka T. 2013. Fundamental properties of substorm time energetic electrons in the innermagnetosphere. *J Geophys Res (Space Phys)* **118**: 1589–1603. https://doi.org/10.1002/jgra.50115.

Evans DS, Greer MS. 2004. *Polar orbiting environmental satellite space environment monitor–2 instrument descriptions and archive data documentation (NOAA Tech. Mem. 1.4)*. Space Environment Laboratory, Boulder, CO, USA.

Gjerloev JW. 2012. The SuperMAG data processing technique. *J Geophys Res* **117**: A09213. https://doi.org/10.1029/2012JA017683.

Gledhill JA. 1986. The effective recombination coefficient of electrons in the ionosphere between 50 and 150 km. *Radio Sci* **21(3)**: 399–408. https://doi.org/10.1029/RS021i003p00399.

Goldberg RA, Jackman CH, Barcus JR, Søraas F. 1984. Nighttime auroral energy deposition in the middle atmosphere. *J Geophys Res (Space Phys)* **89**: A7. https://doi.org/10.1029/JA089iA07p05581.

Hirayama H, Namito Y, Bielajew AF. 2005. *The EGS5 Code System, SLAC-R-730 and KEK Report 2005-8*. URL http://rcwww.kek.jp/research/egs/egs5_manual/slac730-150228.pdf

Imhof WL. 1988. Fine resolution measurements of the L-dependent energy threshold for isotropy at the trapping boundary. *J Geophys Res* **93**: 9743–9752. https://doi.org/10.1029/JA093iA09p09743.

Jaynes AN, Baker DN, Singer H, Rodriguez J, Loto'aniu TM, et al. 2015. Source and seed populations for relativistic electrons: Their roles in radiation belt changes. *J Geophys Res (Space Phys)* **120**: 7240–7254. https://doi.org/10.1002/2015JA021234.

Jelly D, Brice N. 1967. Changes in Van Allen radiation associated with polar substorms. *J Geophys Res* **72(23)**: 5919–5931. https://doi.org/10.1029/JZ072i023p05919.

Jussila JRT, Aikio AT, Shalimov S, Marple SR. 2004. Cosmic noise absotption events associated with equatorward drifting arc during a substorm growth phase. *Ann Geophys* **22**: 1675–1686. https://doi.org/10.5194/angeo-22-1675-2004.

Kasahara S, Yokota S, Mitani T, et al. 2018a. Medium-energy particle experiments – electron analyzer (MEP-e) for the exploration of energization and radiation in geospace (ERG) mission. *Earth Planets Space* **70**: 69. https://doi.org/10.1186/s40623-018-0847-z.

Kasahara Y, Kasaba Y, Kojima H, Yagitani S, Ishikawa K, et al. 2018b. The Plasma Wave Experiment (PWE) onboard the Arase (ERG) satellite. *Earth Planets Space* **70**: 86. https://doi.org/10.1186/s40623-018-0842-4.

Kasahara S, Yokota S, Hori T, Keika K, Miyoshi Y, Shinohara I. 2018c. *Updated daily, The MEP-e instrument Level-2 3-D flux data of Exploration of energization and Radiation in Geospace (ERG) Arase satellite, Version v01.01*. ERG Science Center, Institute for Space-Earth Environmental Research, Nagoya University. https://doi.org/10.34515/DATA.ERG-02000 Accessed 2021-01-01.

Kasahara Y, Kojima H, Matsuda S, Ozaki M, Yagitani S, Shoji M, Nakamura S, Kitahara M, Miyoshi Y, Shinohara I. 2018d. *Updated daily, The PWE/OFA instrument Level-2 spectrum data of Exploration of energization and Radiation in Geospace (ERG) Arase satellite, Version v02.01*. ERG Science CenterInstitute for Space-Earth Environmental Research, Nagoya University. https://doi.org/10.34515/DATA.ERG-08000 Accessed 2021-01-01.

Kataoka R, Nishiyama T, Tanaka Y-M, Kadokura A, Uchida HA, et al. 2019. Transient ionization of the mesosphere during auroral breakup: Arase satellite and ground-based conjugate observations at Syowa Station. *Earth Planet Space* **71**: 9. https://doi.org/10.1186/s40623-019-0989-7.

Kirkwood S, Eliasson L. 1990. Energetic particle precipitation in the sub storm growth phase measured by EISCAT and Viking. *J Geophys Res* **95(A5)**: 6025–6037. https://doi.org/10.1029/JA095iA05p06025.

Kirkwood S, Barabash V, Belova E, Nilsson H, Rao TN, Stebel K, Osepian A, Chilson PB. 2002. Polar mesosphere winter echoes during solar proton events. *Adv Polar Upper Atmos Res* **16**: 111–125. http://doi.org/10.15094/00006351.

Lübken F-J, Singer W, Latteck R, Strelnikova I. 2007. Radar measurements of turbulence, electron densities, and absolute reflectivities during Polar Mesosphere Winter Echoes (PMWE). *Adv Space Res* **40**: 758–764. https://doi.org/10.1016/j.asr.2007.01.015.

Matsuda S, Kasahara Y, Kojima H, Kasaba Y, Yagitani S, et al. 2018. Onboard software of plasma wave experiment aboard Arase: Instrument management and signal processing of waveform capture/onboard frequency analyzer. *Earth Planets Space* **70**: 75. https://doi.org/10.1186/s40623-018-0838-0.

Matsuoka A, Teramoto M, Nomura R, Nose M, Fujimoto A, et al. 2018a. The ARASE (ERG) magnetic field investigation. *Earth Planet Space* **70**: 43. https://doi.org/10.1186/s40623-018-0800-1.

Matsuoka A, Teramoto M, Imajo S, Kurita S, Miyoshi Y, Shinohara I. 2018b. *Updated daily, The MGF instrument Level-2 spin-fit magnetic field data of Exploration of energization and Radiation in Geospace (ERG) Arase satellite, Version v03.03*. ERG Science Center, Institute for Space-Earth Environmental Research, Nagoya University. https://doi.org/10.34515/DATA.ERG-06001; Accessed 2021-01-01.

McKay D, Partamies N, Vierinen J. 2018. Pulsating aurora and cosmic noise absorption associated with growth-phase arcs. *Ann Geophys* **36(1)**: 59–69. https://doi.org/10.5194/angeo-36-59-2018.

Mitani T, Takashima T, Kasahara S, Miyake W, Hirahara M. 2018a. High-energy electron experiments (HEP) aboard the ERG (Arase) satellite. *Earth Planet Space* **70**: 77. https://doi.org/10.1186/s40623-018-0853-1.

Mitani T, Hori T, Park I, Takashima T, Miyoshi Y, Shinohara I. 2018b. *Updated daily, The HEP instrument Level-2 omni-directional flux data of Exploration of energization and Radiation in Geospace (ERG) Arase satellite, Version v03.01*. ERG Science Center, Institute for Space-Earth Environmental Research, Nagoya University. https://doi.org/10.34515/DATA.ERG-01001; Accessed 2021-01-01.

Miyoshi Y, Kataoka R, Kasahara Y, Kumamoto A, Nagai T, Thomsen M. 2013. High-speed solar wind with southward interplanetary magnetic field causes relativistic electron flux enhancement of the outer radiation belt via enhanced condition of whistler waves. *Geophys Res Lett* **40(17)**: 4520–4525. https://doi.org/10.1002/grl.50916.

Miyoshi Y, Oyama S, Saito S, Kurita S, Fujiwara H, Kataoka R, Ebihara Y, Kletzing C, et al. 2015. Energetic electron precipitation associated with pulsating aurora: EISCAT and Van Allen Probe observations. *J Geophys Res Space Phys* **120**: 2754–2766. https://doi.org/10.1002/2014JA020690.

Miyoshi Y, Shinohara I, Takashima T, Kazushi A, Nana Higashio T, et al. 2018a. Geospace exploration project ERG. *Earth Planet Space* **70**: 101. https://doi.org/10.1186/s40623-018-0862-0.

Miyoshi Y, Hori T, Shoji M, Teramoto M, Chang T-F, et al. 2018b. The ERG Science Center. *Earth, Planets, Space* **70**: 96. https://doi.org/10.1186/s40623-018-0867-8.

Miyoshi Y, Shinohara I, Jun C-W. 2018c. *Updated daily, The Level-2 orbit data of Exploration of energization and Radiation in Geospace (ERG) Arase satellite, Version v03*. ERG Science Center, Institute for Space-Earth Environmental Research, Nagoya University. https://doi.org/10.34515/DATA.ERG-12000; Accessed 2021-01-01.

Miyoshi Y, Hosokawa K, Kurita S, Oyama S-I, Ogawa Y, et al. 2021. Penetration of MeV electrons into the mesosphere accompanying pulsating aurorae. *Sci Rep* **11**: 13724. https://doi.org/10.1038/s41598-021-92611-3.

Nishimura Y, Lessard M, Katoh Y, Miyoshi Y, Grono E, et al. 2020. Diffuse and pulsating aurora. *Space Sci Rev* **216**: 4. https://doi.org/10.1007/s11214-019-0629-3.

Nishiyama T, Sato K, Nakamura T, Tsutsumi M, Sato T, Kohma M, Nishimura K, Tomikawa Y, Ejiri MK, Tsuda TT. 2015. Height and time characteristics of seasonal and diurnal variations in PMWE based on 1 year observations by the PANSY radar (69.0°S, 39.6°E). *Geophys Res Lett* **42**: 2100–2108. https://doi.org/10.1002/2015GL063349.

Nishiyama T, Sato K, Nakamura T, Tsutsumi M, Sato T, Tanaka Y-M, Nishimura K, Tomikawa Y, Kohma M. 2018. Simultaneous observations of polar mesosphere winter echoes and cosmic noise absorptions in a common volume by the PANSY radar (69.0°S, 39.6°E). *J Geophys Res (Space Phys)* **123**: 5019–5032. https://doi.org/10.1029/2017JA024717.

Oyama S, Kero A, Rodger CJ, Clilverd MA, Miyoshi Y, Partamies N, Turunen E, Raita T, Verronen PT, Saito S. 2017. Energetic electron precipitation and auroral morphology at the substorm recovery phase. *J Geophys Res (Space Phys)* **122**: 6508–6527. https://doi.org/10.1002/2016JA023484.

Pesnell WD, Goldberg RA, Jackman CH, Chenette DL, Gaines EE. 1992. A search of UARS data for ozone depletions caused by the highly relativistic electron precipitation events of May 1992. *J Geophys Res* **104**: A1. https://doi.org/10.1029/1998JA900030.

Picone JM, Hedin AE, Drob DP, Aikin AC. 2002. NRLMSISE-00 empirical model of the atmosphere: Statistical comparisons and scientific issues. *J Geophys Res* **107(A12)**: 1468. https://doi.org/10.1029/2002JA009430.

Pytte T, Trefall H, Kremser G, Jalonen L, Riedler W. 1976. On the morphology of energetic (≥30 keV) electron precipitation during the growth phase of magnetospheric substorms. *J Atmos Sol-Terr Phys* **38(7)**: 739–755. https://doi.org/10.1016/0021-9169(76)90112-4.

Ranta H, Ranta A. 1981. Development of the auroral absorption substorm: Studies of pre-onset phase and sharp onset using an extensive riometer network. *Planet Space Sci* **29**: 1287–1313. https://doi.org/10.1016/0032-0633(81)90095-7.

Rossberg L. 1976. Prebay electron precipitation as seen by balloons and satellites. *J Geophys Res* **81(19)**: 3437–3440. https://doi.org/10.1029/JA081i019p03437.

Sato K, Tsutsumi M, Sato T, Nakamura T, Saito A, Tomikawa Y, Nishimura K, Kohma M, Yamagishi H, Yamanouchi T. 2014. Program of the Antarctic Syowa MST/IS radar (PANSY). *J Atmos Sol Terr Phys* **118(Part A)**: 2–15. https://doi.org/10.1016/j.jastp.2013.08.022.

Sato T, Iwamoto Y, Hashimoto S, Ogawa T, Furuta T, et al. 2018. Features of Particle and Heavy Ion Transport code System (PHITS) version 3.02. *J Nucl Sci Technol* **55**: 684–690. https://doi.org/10.1080/00223131.2017.1419890.

Seppälä A, Clilverd MA, Beharrell MJ, Rodger CJ, Verronen PT, Andersson ME, Newnham DA. 2015. Substorm-induced energetic electron precipitation: Impact on atmospheric chemistry. *Geophys Res Lett* **42**: 8172–8176. https://doi.org/10.1002/2015GL065523.

Sergeev VA, Sazhina EM, Tsyganenko NA, Lundblad JA, Soraas F. 1983. Pitch-angle scattering of energetic protons in the magnetotail current sheet as the dominant sources of their isotropic precipitation into the nightside ionosphere. *Planet Space Sci* **31**: 1147–1155. https://doi.org/10.1016/0032-0633(83)90103-4.

Sergeev V, Nishimura Y, Kubyshkina M, Angelopoulos V, Nakamura R, Singer H. 2012. Magnetospheric location of the equatorward prebreakup arc. *J Geophys Res* **117**: A01212. https://doi.org/10.1029/2011JA017154.

Shepherd SG. 2014. Altitude-adjusted corrected geomagnetic coordinates: Definition and functional approximations. *J Geophys Res (Space Phys)* **119**: 7501–7521. https://doi.org/10.1002/2014JA020264.

Sivadas N, Semeter J, Nishimura Y, Kero A. 2017. Simultaneous measurements of substorm-related electron energization in the ionosphere and the plasma sheet. *J Geophys Res (Space Phys)* **122**: 10528–10547. https://doi.org/10.1002/2017JA023995.

Sivadas N, Semeter J, Nishimura YT, Mrak S. 2019. Optical signatures of the outer radiation belt boundary. *Geophys Res Lett* **46**: 8588–8596. https://doi.org/10.1029/2019GL083908.

Tanaka T. 2015. Substorm auroral dynamics reproduced by advanced global magnetosphere–ionosphere (M–I) coupling simulation. In: *Auroral dynamics and space weather*, Geophys Monogr Ser. vol **215**, Zhang Y, (Ed.) AGU, Washington, DC. pp. 177–190. https://doi.org/10.1002/9781118978719.ch13.

Tanaka YM, Nishiyama T, Kadokura A, Ozaki M, Miyoshi Y, et al. 2019. Direct comparison between magnetospheric plasma waves and polar mesosphere winter echoes in both hemispheres. *J Geophys Res* **124(11)**: 9626–9639. https://doi.org/10.1029/2019JA026891.

Tesema F, Partamies N, Nesse Tyssøy H, McKay D. 2020. Observations of precipitation energies during different types of pulsating aurora. *Ann Geophys* **38**: 1191–1202. https://doi.org/10.5194/angeo-38-1191-2020.

Tsyganenko NA. 1996. *Effect of the solar wind conditions on the global magnetospheric configuration as deduced from data-based field models (European Space Agency SP-389)*. European Space Agency Publication, Paris. 181 p.

Uchida HA, Kataoka R, Kadokura A, Murase K, Yukimatu AS, et al. 2020. Asymmetric development of auroral surges in the northern and southern hemispheres. *Geophys Res Lett* **47(13)**: e2020GL088750. https://doi.org/10.1029/2020GL088750.

van de Kamp M, Rodger CJ, Seppälä A, Clilverd MA, Verronen PT. 2018. An updated model providing long-term data sets of energetic electron precipitation, including zonal dependence. *J Geophys Res (Atmos)* **123**: 9891–9915. https://doi.org/10.1029/2017JD028253.

Yamamoto M, Tsuda T, Kato S, Sato T, Fukao S. 1987. A saturated inertia gravity wave in the mesosphere observed by the middle and upper atmosphere radar. *J Geophys Res* **92**: 11993–11999.

Appendix A

Summary of mesospheric ionization events below the altitude of 70 km

Table A1. List of the mesospheric echoes at <70 km altitude identified by the PANSY radar during substorms. "Arase conjunction" indicates whether the footprints are located at ±5° in magnetic latitude and ±1 MLT from Syowa Station at the timing of the echoes. "Aurora data" represents whether the sky is clear and the data of the all-sky imager is available. "Substorm phase" is determined from the local magnetic field variation and the all-sky images of aurora. "Max SME" shows peaks of SME index (Gjerloev, 2012) of the substorms.

#	Date (yyyy-mm-dd)	Time (UT)	Arase conjunction	Aurora data	Substorm phase	Max SME [nT]	comments
1	2017-05-25	23:05 23:30	○	○	growth expansion	211	Event #2
2	2017-06-17	23:40	○	×	expansion	673	
3	2017-06-30	22:20	○	○	expansion	411	Reported by Kataoka et al. (2019
4	2017-07-11	23:30	×	×	expansion	463	
5	2017-07-21	23:40	×	○	expansion	641	
6	2017-07-23	00:20	×	○	recovery	559	
7	2017-08-06	00:50	×	×	unclear	792	
8	2017-09-07	20:45	×	○	growth	3510	During a solar proton event
9	2017-09-08	00:20	×	○	unclear	4455	
10	2017-09-10	21:50	×	○	unclear	666	During a solar proton event
11	2017-09-11	22:50	×	×	expansion	552	During a solar proton event
12	2018-03-23	23:10	×	○	recovery	865	
13	2018-03-24	00:30	×	○	recovery	865	
14	2018-04-11	01:15 02:05	×	○	expansion recovery	1121	
15	2018-05-06	22:05	×	○	expansion	1121	
16	2018-06-02	01:40 02:00	×	×	unclear	1332	
17	2018-06-07	21:25	×	○	expansion	180	
18	2018-06-26	20:15	×	×	expansion	597	
19	2018-06-27	22:20 00:15	×	×	expansion unclear	256 261	
20	2018-07-24	23:55	○	○	growth - expansion	365	Event #1
21	2018-07-25	21:10	×	○	expansion	328	
22	2018-08-21	23:50	○	○	unclear	363	
23	2018-08-27	20:15 22:00	×	×	growth recovery	698	
24	2018-08-29	00:10	×	×	expansion	329	
25	2018-08-30	20:05	×	×	unclear	401	

Appendix B

Conservation of the loss-cone flux per unit solid angle

In this section, we consider the scaling factor for converting particle fluxes in the magnetosphere to that at the top of the atmosphere (TOA). The following assumptions are taken into consideration:

1. The pitch-angle distribution is isotropic at the TOA.
2. The number of particles in the loss-cone angle that pass through a surface of a given magnetic flux tube per unit time is conserved.

First, the loss-cone flux in the magnetosphere, F_{mag}, in $\mathrm{cm}^{-2}\mathrm{s}^{-1}$ is written as

$$F_{\mathrm{mag}} = \int_{\theta=0,\alpha_{\mathrm{loss}}} \overline{f_{\mathrm{mag}}} \cos\theta \, d\Omega,$$

where $\overline{f_{\mathrm{mag}}}$, θ, and $\mathrm{d}\Omega$ are the solid-angle averaged flux per unit solid angle inside the loss cone, pitch angle, and the solid-angle element, respectively. We get

$$F_{\mathrm{mag}} = \overline{f_{\mathrm{mag}}} \int_{0^\circ}^{\alpha_{\mathrm{loss}}} \cos\theta \sin\theta \mathrm{d}\theta \int_{0^\circ}^{360^\circ} \mathrm{d}\phi = \pi \overline{f_{\mathrm{mag}}} \sin^2 \alpha_{\mathrm{loss}}. \tag{B1}$$

From the assumption (B1), the loss-cone flux at the TOA, F_{TOA}, in $\mathrm{cm}^{-2}\mathrm{s}^{-1}$ is written as

$$F_{\mathrm{TOA}} = \pi f_{\mathrm{TOA}}. \tag{B2}$$

From the assumption (B2), we obtain

$$S_{\mathrm{mag}} F_{\mathrm{mag}} = S_{\mathrm{TOA}} F_{\mathrm{TOA}} \Longleftrightarrow F_{\mathrm{TOA}} = \frac{S_{\mathrm{mag}}}{S_{\mathrm{TOA}}} F_{\mathrm{mag}},$$

where S is the area of a given flux tube. From the equations (B1) and (B2), the above equation can be written as

$$f_{\mathrm{TOA}} = \frac{S_{\mathrm{mag}}}{S_{\mathrm{TOA}}} \overline{f_{\mathrm{mag}}} \sin^2 \alpha_{\mathrm{loss}}.$$

Considering the conservation of magnetic fluxes ($S_{\mathrm{mag}}\, B_{\mathrm{mag}} = S_{\mathrm{TOA}}\, B_{\mathrm{TOA}}$),

$$\Longleftrightarrow f_{\mathrm{TOA}} = \frac{B_{\mathrm{TOA}}}{B_{\mathrm{mag}}} \overline{f_{\mathrm{mag}}} \sin^2 \alpha_{\mathrm{loss}},$$

where B represents the magnetic field strength. Applying the conservation of the first adiabatic invariant ($B_{\mathrm{TOA}}/B_{\mathrm{mag}} = 1/\sin^2\alpha_{\mathrm{loss}}$) for the above equation, we reach the simple conclusion,

$$f_{\mathrm{TOA}} = \overline{f_{\mathrm{mag}}},$$

that the isotropic flux at TOA is the same as the average loss-cone flux at magnetosphere. We also note that the flux F in $\mathrm{cm}^{-2}\mathrm{s}^{-1}$ can be written as $F = \pi f$ using the flux per unit solid angle, f, as obtained from equation (B2).

Appendix C

Observations by the Arase satellite for Event #2 on May 25–26, 2017

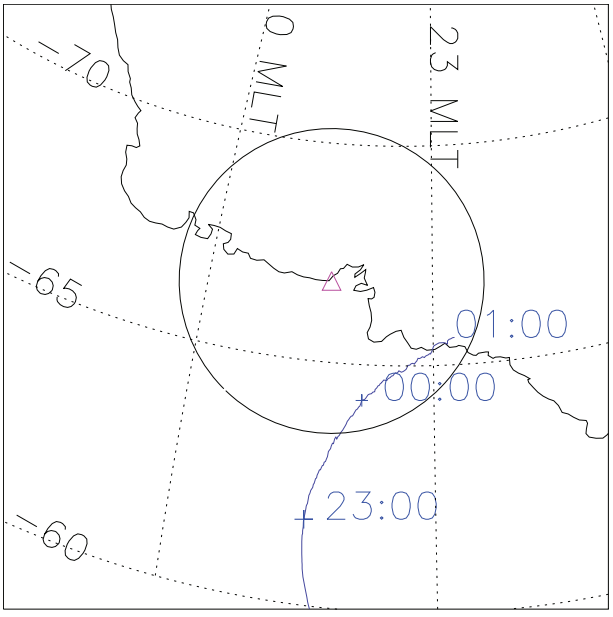

Figure C1. Footprints of the Arase satellite during EEP event #2 on May 25–26, 2017, in the AACGM coordinate. The mapped altitude is 100 km. The magnetic local times are calculated at 2307 UT on May 25. The footprints of the Arase satellite were traced using the T96 model. The black circle indicates the all-sky field of view at Syowa Station, assuming a 10° elevation angle and an emission altitude of 110 km.

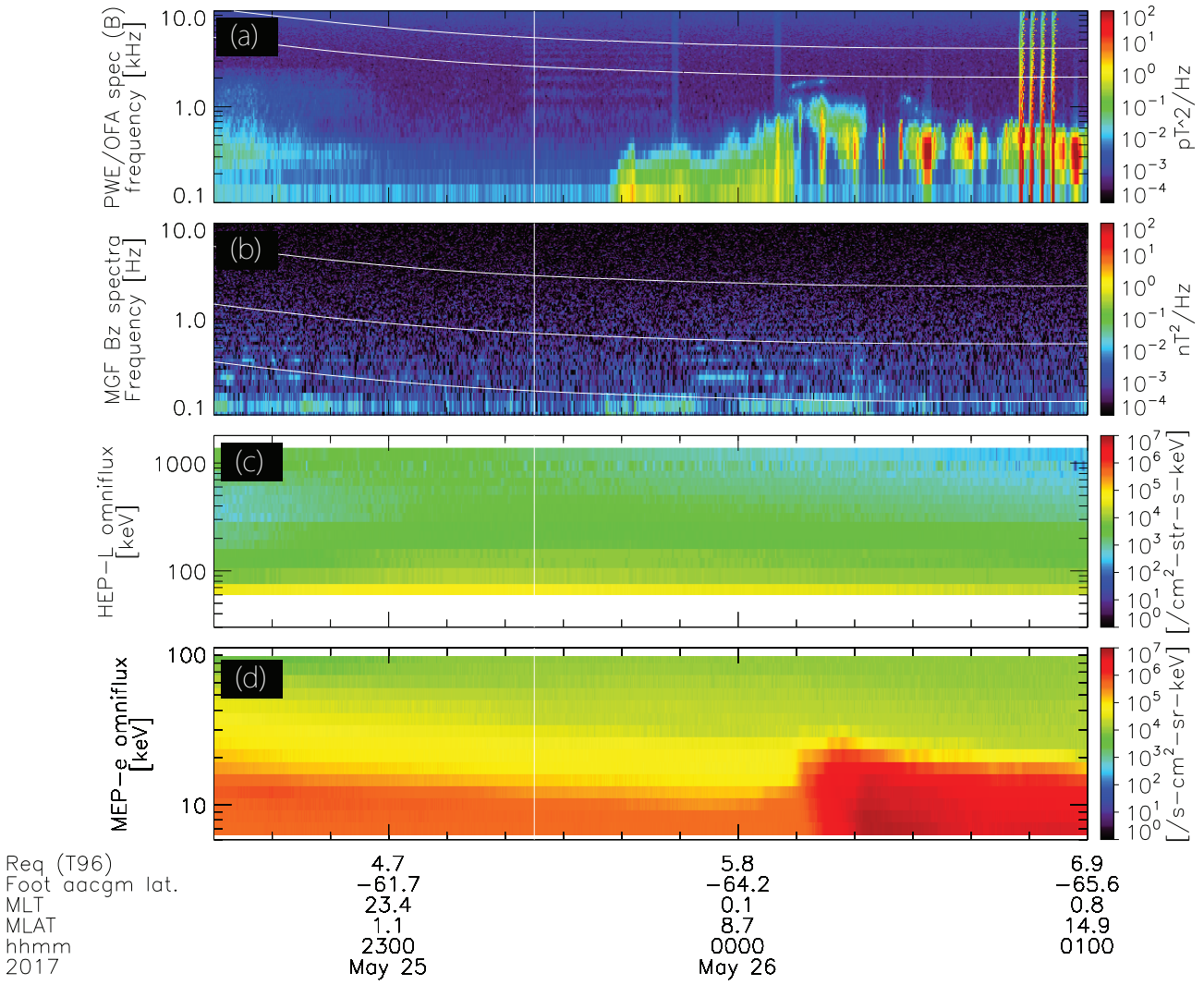

Figure C2. In-situ observation of plasma waves and energetic electrons at the Arase satellite for the same time period as shown in Figure 7.

Cite this article as: Murase K, Kataoka R, Nishiyama T, Nishimura K, Hashimoto T, et al. 2022. Mesospheric ionization during substorm growth phase. *J. Space Weather Space Clim.* **12**, 18. https://doi.org/10.1051/swsc/2022012.